Carbohydrate Polymer Technologies and Applications 10 (2025) 100711

Contents lists available at ScienceDirect

Carbohydrate Polymer Technologies and Applications

journal homepage: www.sciencedirect.com/journal/carbohydrate-polymer-technologies-and-applications

Development of clay/alginate/chondroitin sulfate composite microspheres via continuous process for chronic wounds regeneration

Cristian Nomicisio [a], Marco Ruggeri [a], Christine Taviot-Guého [b], Cinzia Boselli [a], Antonia Icaro Cornaglia [c], Eleonora Bianchi [a], Elena Del Favero [d], Caterina Ricci [d], Giuseppe Firpo [e], Barbara Vigani [a], Paolo Vacca [f], César Viseras [g], Silvia Rossi [a], Giuseppina Sandri [a,*]

[a] Department of Drug Sciences, University of Pavia, Viale Taramelli 12, 27100 Pavia, Italy
[b] Institut de Chimie de Clermont-Ferrand, Université Clermont-Auvergne, UMR CNRS 6296, 24 av Blaise Pascal, 63171 Aubière, France
[c] Department of Public Health, Experimental and Forensic Medicine, University of Pavia, via Forlanini 2, 27100, Pavia, Italy
[d] Department of Medical Biotechnology and Translational Medicine, University of Milano, LITA, Via Fratelli Cervi 93, 20090 Segrate MI Italy
[e] Department of Physics, Nanomedicine Laboratory, University of Genoa, Via Dodecaneso 33, 16146 Genoa, Italy
[f] SAES Getters SpA, Viale Italia 77, Lainate MI, Italy
[g] Department of Pharmacy and Pharmaceutical Technology, Faculty of Pharmacy, University of Granada, Campus of Cartuja, 18071 Granada, Spain

ARTICLE INFO

Keywords:
Alginate
chondroitin sulfate
Layered double hydroxides
Composite materials
3D scaffolds
Wound healing
Tissue engineering

ABSTRACT

Chronic wounds significantly affect the quality of life of millions of people, generating substantial problems for the patients and for health care systems. Therefore, this work focuses on the development of microparticles based on alginate and chondroitin sulfate which were doped with layered double hydroxides (LDH), anionic clay minerals, based on Zn and Al. The obtained clay/polysaccharide composite materials could provide enhanced properties for wound healing, in particular related to cell adhesion and proliferation. The microparticles were manufactured by spray drying and crosslinked using $CaCl_2$ to obtain insoluble scaffolds for application in the physiological environment. The materials and the process were chosen continuous manufacturing in the industrial field. The mean diameter of the obtained microparticles ranged from 10 to 15 μm with a narrow dimensional distribution. Solid state characterizations (XRD, FTIR, SAXS, TGA/DSC) confirmed the LDH doping in a concentration of around 5 %w/w. The presence of LDH enhanced the stability of the systems in aqueous environment, increasing the wettability and decreasing the zeta potential due to their positive charge. Preclinical in vitro studies suggested a positive impact of LDH doping which led to a cell proliferation increase of around 15 %. In vivo studies demonstrated the safety and efficacy of the systems, suggesting the potential of this platform for therapeutic use.

1. Introduction

Chronic wounds impact around 40 million individuals globally, creating major financial strains on health-care systems and, eventually, on the country's economy (Heras et al., 2020). The most common therapeutic strategies have proven ineffective for the treatment of chronic wounds. Therefore, the design and development of innovative healing devices is required (Pei et al., 2023). For this reason, biodegradable three-dimensional matrices, known as scaffolds, are used, as they convey biochemical signals that regulate cell behavior, allow nutrients and oxygen to permeate, and offer mechanical and structural support. Composite or hybrid materials with fibrous or porous structures, alongside micro and nanoparticles, are employed to promote fast and scarless wound healing. They can also be doped with functional agents to provide a synergic activity in the treatment (Molina et al., 2021; Nosenko et al., 2018).

For decades, clay minerals have been used in medicine to cure wounds, stop bleeding, and provide anti-inflammatory effects (Dong et al., 2021). Their biocompatibility, non-toxic degradation products, and positive effects on cell adhesion, proliferation, and differentiation indicate their remarkable potential for the manufacturing of novel bioactive scaffolds (Mousa et al., 2018; Ruggeri et al., 2024). Research

* Corresponding author at: Department of Drug Sciences, University of Pavia, Viale Taramelli 12, 27100 Pavia, Italy.
E-mail address: g.sandri@unipv.it (G. Sandri).

https://doi.org/10.1016/j.carpta.2025.100711

Available online 13 February 2025

has shown that clays, particularly when combined with polymeric systems, result in improved mechanical properties, quicker tissue regeneration owing to increased collagen deposition, and skin re-epithelialization with minimal scarring (Miele et al., 2023; Rajeshkumar et al., 2021). Although clay minerals are abundant in nature, different synthetic clays have been produced to meet specific demands in industry. In this way more homogenous structures and chemical compositions, larger uniformity in terms of particle size, impurities, and water content, and absence of microbial contamination can be achieved (Ghadiri et al., 2015). Among the synthetic clays, layered double hydroxides (LDH) have important features that are helpful in the tissue regeneration process. The structure of LDH is made of positively charged brucite-like layers containing divalent and trivalent cations, which are octahedrally coupled to six OH hydroxyl groups. Interchangeable anions and water molecules are present between the layers, balancing their positive charge (Ameena Shirin et al., 2021). Due to their advantageous properties like anion exchange, LDH have been combined with polymers to produce drug delivery systems and even platforms for tissue engineering (Nomicisio et al., 2023). In fact, LDH-based materials provide several benefits for biomedical applications due to their adaptable chemical composition, minimal cytotoxicity and good biocompatibility. Moreover, LDH can gradually degrade through hydrolysis in acidic environments, releasing their metal cations (Hu et al., 2022). Therefore, the type of the metal cation and its concentration (which is susceptible to variation based on the solubilization rate), determine the intrinsic active features of LDH. Additionally, it has been shown that the LDH structure alone, with no intercalated drugs, is responsible for enhancing the immunomodulating activity and promoting neovascularization and angiogenesis. This allows the chemical composition of LDH layers to be tailored to the therapeutic purpose (Constantino et al., 2023).

Given these premises, the aim of this work is the development of polymeric microparticles doped with LDH to be used as powder for cutaneous application in the treatment of chronic wounds. Due to the high number of patients suffering from chronic wounds, the need of continuous methods for scaffold production is high. Green technologies should be implemented in the manufacturing process, further facilitating the scale-up and the industrial success of this type of structure. Therefore, special attention has been given to sustainable methods and materials that enable industrial production.

In continuous manufacturing, raw materials continuously feed the process, resulting in the final products, whereas, in batch manufacturing, starting materials are loaded at the beginning of the process and the final product is recovered all at once. Any material produced at any stage should therefore be directly transferred in the next step for further processing, ensuring fast and streamlined operations (Lee et al., 2015). This allows for better process control, decreased variability, and increased scalability. The EMA guidelines on continuous manufacturing also include the possibility of a set up with hybrid modes wherein some unit operations operate in batch and some continuously or a fully integrated system where every step connects and runs continuously (ICH, 2023).

In the present work, different techniques are used and possibly combined in series to obtain a continuous process. The LDH were produced using the co-precipitation method following green and more sustainable approaches which did not require final purification and washing, allowing the reduction of synthetic steps and chemical wastes (Nomicisio et al., 2024). This led to high quality products, which could be potentially recovered continuously and subsequently used to produce the microparticles. At this purpose, spray drying was chosen as an optimal technique which has proven to be extremely appealing for both laboratory and industrial scale. It is a fast, repeatable, versatile, continuous, and one-step technique, which allows to obtain small and uniform particles, making it scalable without substantial adaptations. In addition, the spray drying method could easily avoid the use of organic solvents as a green process (Ma et al., 2020; Sosnik & Seremeta, 2015).

Concerning the materials that were used to produce the polymeric matrix, alginate and chondroitin sulfate were selected. Alginate (ALG) has numerous beneficial properties for wound healing, such as biocompatibility, biodegradability, low-immunogenicity and toxicity, antiseptic properties, optimal water vapor transmission rate, and relatively low cost (Sahoo & Biswal, 2021). Chondroitin sulfate (CS) is a glycosaminoglycan and a main component of the extracellular matrix (ECM). It can substantially enhance cell proliferation, the expression of various fibroblast growth factors and collagen synthesis, while down-regulating the inflammatory factors, and inhibiting cell apoptosis (Wu et al., 2022). The evaluation of the optimal ratio between alginate/chondroitin sulfate was carried out, in order to assess the correlation with the physico-chemical and biological properties of the scaffolds.

The LDH were used to dope the microparticles in order to further promote the restoration of the damaged skin tissue. LDH meet all of the requirements needed for both industrial scale production and sustained application development, including relative affordability and availability of precursors, cost-effective manufacturing, and non-toxicity for a wide range of chemical compositions (Dazon et al., 2023). Their chemical composition was tailored by choosing Zn and Al as the main cations in the structure. Zinc is, in fact, essential for controlling all stages of wound healing, including angiogenesis, membrane regeneration, oxidative stress, coagulation, inflammation and immunological defense, and scar formation (Lin et al., 2017). Moreover, the LDH were produced using the co-precipitation method following green and more sustainable approaches, which led to high quality products reducing the synthetic steps and the chemical wastes (Nomicisio et al., 2024).

2. Materials and methods

2.1. Materials

Zinc nitrate ($Zn(NO_3)_2 \times 6H_2O$, pur. 98 %, Acros Organics, France), aluminium nitrate ($Al(NO_3)_3 \times 9H_2O$, pur. 99 %, Sigma Aldrich, France) and a 25 % NH_4OH solution (Sigma Aldrich, France) were used for the ZnAl LDH synthesis. Alginic acid (sodium salt) (ALG) from brown algae (low viscosity) (Sigma Aldrich, Italy) and chondroitin sulfate 100 EP (CS) low MW (12-14 kDa), mixture of A (chondroitin 4 sulfate) and C (chondroitin 6 sulfate), (Bioiberica, Barenz, Milan, Italy) were used as polymers. $CaCl_2$ (Sigma Aldrich, Italy) was used as crosslinking agent.

2.2. Methods

2.2.1. LDH synthesis

The ZnAl LDH (chemical formula $Zn_2Al(OH)_6(NO_3)\times 2H_2O$) were synthesized using the co-precipitation method as previously reported (Nomicisio et al., 2024). Briefly, 20 mL of a 1 M solution of zinc nitrate and aluminum nitrate was added dropwise at a constant flow rate (0.67 ml/min) by means of a peristaltic pump in a reactor previously filled with 100 ml of deionized water at room temperature, under N_2 atmosphere and upon magnetic stirring. The pH value of the reaction was maintained constant at 8 and controlled by the addition of a 2 M NH_4OH solution. The total addition time was set to 30 mins followed by 1 h of aging. Then, the precipitate was recovered through centrifugation (4500 rpm for 10 mins). The supernatant was withdrawn and the resulting LDH were used as a slurry without further purification.

2.2.2. Preparation of the microparticles

The obtained LDH were resuspended in deionized water and alginate and chondroitin sulfate were added to the mixture. Then, the LDH-containing suspension was spray-dried using a Mini Spray Dryer (Buchi B-190, Büchi Labortechnik AG, Essen, Germany) equipped with a PT-100 temperature probe, 911–400 woven polyester fabric suction filter, peristaltic pump and 0.5 mm diameter nozzle. The polymeric blends were sprayed as atomized droplets under 600 ml/h co-current feed air flow rate at 200 °C inlet air temperature (130 °C outlet air temperature). The microparticles were collected in the reservoir after

immediate drying, with a process yield that was always higher than 50 %. The composition of the obtained microparticles is reported in Table 1. The microparticles were then cross-linked using $CaCl_2$ following a protocol reported in literature (Cui et al., 2017). Briefly, the microparticles were first dispersed in 96 % ethanol for 5 mins, then transferred to a 2 % $CaCl_2$ ethanolic solution for 20 mins and afterwards to a 40 % $CaCl_2$ aqueous solution for 2 h. Finally, the microparticles were washed twice using deionized water to remove the excess of $CaCl_2$. After recovering the microparticles through centrifugation, they were placed overnight at 40 °C to eliminate the excess water.

A preformulation study was carried out to optimize the ratio between ALG and CS and the spray-drying process (data not shown). An increase in ALG led to partial aggregation of the particles, probably related to the increased solution viscosity which impaired the spray drying process. As the amount of CS was increased, the microparticles were not structurally stable as they partially collapsed. Moreover, it is optimal for the system to consist in a larger amount of ALG compared to CS to facilitate the crosslinking process with $CaCl_2$.

Therefore, the optimal ratios between ALG/CS for microparticle production were found. The composition of the obtained dried microparticles is reported in Table 1.

Concerning the spray drying process, the parameters of temperature, solution feed rate and air flow rate were varied to limit material loss on the walls of the spray drying chamber and to increase the process yield (data not shown). A temperature reduction did not allow a sufficient yield as a fast and complete evaporation was not totally achieved, while a decrease in flow rate did not optimally allow the droplet formation. Both parameters were crucial for the obtainment of structurally stable particles.

2.2.3. Physico-chemical and structural characterizations

The morphology of the microparticles was assessed by SEM (Tescan, Mira3XMU, Brno, Czech Republic) before and after crosslinking. The EDX analysis on the crosslinked microparticles was also performed. The samples were placed on metal stubs through a double-adhesive tape and sputtered by means of the vacuum deposition of graphite.

To further investigate the clay distribution in the microparticles, SEM was coupled with a focused ion beam (FIB) (CrossBeam 1540 XB Carl Zeiss, Oberkochen, Germany). FIB generates and directs a stream of gallium ions onto the sample as a method of imaging. The microparticles were therefore cross-sectioned in order to reveal the internal morphology. In addition, linear EDX analyses were performed on the sectioned particles to assess the elemental distribution.

Small Angle X-ray Scattering analysis on the nanoscale was performed at the European Synchrotron Radiation Facility (ESRF, Grenoble, France), carrying out experiments with the ID02 beamline. Samples were inserted in 2-mm polycarbonate capillaries (ENKI, Italy) and fully hydrated with water. The scattered radiation was collected at two different sample-to-detector distances (1 m and 10 m), to investigate a wide range of q. The scattering vector q is defined as $q = (4\pi \sin\theta)/\lambda$, where θ is the scattering angle and λ is the wavelength of the X-rays, in our configuration $0.006 < q < 7.5\ nm^{-1}$ and λ =0.1 nm.

The particle size distribution was determined using the laser diffraction technique by means of a Mastersizer 3000E particle size meter (Malvern Instruments, Milan, Italy). The microparticles were suspended in isopropanol to avoid possible swelling. The particle diameters (d10, d50, d90) were derived from the cumulative volume distribution, and the distribution width (Span= (d90 – d10)/d50) was calculated.

XRD analyses were performed on a Philips X'Pert Pro diffractometer (France) equipped with a 1D X'celerator detector (active length 2.122°), using a Cu $K_{\alpha1}/K_{\alpha2}$ source (λ = 1.5405 Å) in a θ−θ Bragg−Brentano geometry from 2 to 70°(2θ) with a scan pitch of 0.016°. The FullProf Suite software was used for profile matching and phase identification.

Fourier transform infrared (FT-IR) spectra were recorded on a Nicolet iS20 spectrometer from Thermo Scientific in absorbance mode using the ATR (attenuated total reflectance) detection mode over the wavenumber domain of 400 to 4000 cm^{-1}. 128 scans were collected for each spectrum at a resolution of 4 cm^{-1}.

Thermogravimetric analyses (TGA) and Differential Scanning Calorimetry (DSC) were performed using a TGA 2 (Mettler Toledo) under air flow of 10 ml/min in the temperature range of 25−1000 °C with a linear temperature ramp of 10 °C/min.

2.2.4. In vitro degradation

To assess the degradation of the crosslinked microparticles, suspensions at a concentration of 20 mg/ml were prepared in MilliQ water and placed at 37 °C. After 3 and 6 days, the microparticles were collected through centrifugation (4500 rpm for 10 mins) and dried in an oven at 40 °C overnight after the withdrawal of the supernatant. The weight residue (%) was calculated as the ratio between the weight after degradation and the initial weight.

The morphology of the crosslinked microparticles was also examined through SEM analysis using a Phenom Pure G6 (Alfatest, Cernusco sul Naviglio, Italy).

2.2.5. Zn^{2+} release

The release of Zn^{2+} over time was assessed to evaluate the potential beneficial activity of this cation towards wound healing. At this purpose, the microparticles were suspended in MilliQ water at a concentration of 20 mg/ml and placed at 37 °C in an oscillating water bath. At prefixed times (3, 6 and 18 days), the suspensions were centrifuged (4500 rpm for 10 mins) and the supernatants were recovered and replaced with fresh water to keep the volume constant. The collected supernatants were then analyzed using Zn^{2+}quantification kit (abcam, Prodotti Gianni Srl, Milan, Italy) following the manufacturer's instructions. Briefly, in a 96-well plate, 50 µL of the appropriately diluted supernatant were mixed with 50 µl of Zn^{2+}detection buffer. Samples were incubated in the dark for 10 min at room temperature and fluorescence (λ_{ex}= 485 nm and λ_{em}=525 nm) was then measured with a FLUOstar Omega spectrometer, UV/vis (multimode microplate reader, BMG Labtech, Euroclone SPA, Milan, Italy). A calibration curve between 0 and 100 µM was constructed with an obtained R^2 value always greater than 0.99.

2.2.6. Surface zeta potential

The surface zeta potential (ζ) was determined through SurPASS™ 3 (Anton Paar, Turin, Italy) using a cylindrical cell. A set amount (30 mg) of microparticles was placed between two paper filter disks in the cylindrical cell. A 0.1 M KCl solution was used as the streaming solvent and the ζ was obtained at physiological pH.

2.2.7. Contact angle measurements

The wettability of the systems was evaluated to simulate the behaviour of microparticles in a physiological environment and to consider the impact of clays on the hydrophilicity of materials. At this purpose, the microparticles were compressed using a hydraulic press (1.5 tons for 20 s) to generate discs with a thickness of 0.6 mm.

The measurements were performed using a contact angle meter (DMe-211 Plus, Kyowa, Osaka, Japan) coupled with FAMAS software (Enco, Spinea, Italy) in timed mode to study the variation of the contact angle over time (100, 500 and 1000 ms).

Table 1
Quali-quantitative compositions of the spray-dried microparticles.

Sample	ALG concentration (%w/w)	CS concentration (% w/w)	ZnAl LDH concentration (%w/w)
A2	66.6 %	33.3 %	–
A2-LDH	63.3 %	31.7 %	5 %
A3	75 %	25 %	–
A3-LDH	71.25 %	23.75 %	5 %

2.2.8. Cell proliferation

A cell proliferation assay was performed using Normal Human Dermal Fibroblasts (NHDF, from juvenile foreskin, PromoCell, WVR, Milan, Italy). Fibroblasts (3rd-6th passages) were cultured in Dulbecco's modified Eagle medium (DMEM, Sigma Aldrich, Italy) supplemented with 10 % fetal bovine serum (FBS, Euroclone, Milan, Italy), with 200 IU/ml penicillin/0.2 mg/mL streptomycin (Sigma Aldrich, Milan, Italy), and kept at 37 °C in a 5 % CO_2 atmosphere with 95 % relative humidity (RH). Fibroblasts were seeded in a 96-well plate at 1.5×10^4 cells/well. After 24 h, the microparticles were suspended in the growth medium at different concentrations (0.5–10 mg/ml) and put in contact with the cell substrates. NHDF grown in standard conditions were used as control (GM). After 3 and 6 days of growth, the alamarBlue™ assay was performed to assess the cell proliferation. For the test, the medium containing the microparticles was withdrawn and the cells were washed twice with PBS to remove the residues. Subsequently, 100 µl of an alamarBlue™ solution (10 % v/v in DMEM without phenol red) was added to each well and incubated at 37 °C for 3 h. Fluorescence was measured using a FLUOstar Omega microplate reader (λ_{ex}= 560 nm and λ_{em}=590 nm). Cell viability was expressed as fluorescence intensity (FI) and compared to the control.

2.2.9. Safety and efficacy of the systems in vivo

The in vivo tests were executed in full compliance with the standard international ethical guidelines (European Communities Council Directive 86/609/EEC) approved by Italian Health Ministry (D.L. 116/92). The Local Institutional Ethics Committee of the University of Pavia for the use of animals and the ISS (Istituto Superiore di Sanità) approved the protocol that was used. 9 male rats (Wistar 200–250 g, Envigo RMS S.r. l.) underwent anesthesia using equitensine at 3 ml/kg (39 mM pentobarbital, 256 mM chloral hydrate, 86 mM $MgSO_4$, 10 % v/v ethanol, and 39.6 % v/v propylene glycol) and were subsequently shaven on their back. To test the safety, a subcutaneous implant was performed on the back of each rat through an 8 mm incision and around 20 mg of microparticles were inserted in the incisions, which were then sutured using strips (Steri-Strip Suture, Italy). After 18 days, full thickness biopsies were taken around the incisions and the histological analysis was performed. A biopsy of intact skin was also considered as a positive control. Furthermore, to test the efficacy, on the back of the animals, three circular full thickness burns (diameter of 4 mm) were generated through contact with an aluminum rod (105 °C for 40 s). After 24 h, a 4 mm diameter biopsy punch was used to remove the formed blisters and to get full-thickness lesions. Subsequently, around 20 mg of microparticles were gently applied on the lesion, making sure that the whole area was completely covered, and moistened with 20 µl of saline solution (0.9 g/l). Negative controls were obtained using lesions treated with 20 µl of saline solution. A sterile gauze was used to cover the lesions, and a surgery stretch was applied on the back of the rat (Safety, Italy). At prefixed times (0, 3, 7, 10, 14 and 18 days) the healing process was monitored through the acquisition of digital photographs (Sigma SD 14) which allowed for the measurement of the size of the wounded area (Image J, ICY, Institute Pasteur, France). 18 days after the treatment, the rats were sacrificed following the procedure that was approved in the protocol. Full thickness biopsies, both of the tissue around the initial lesions and of intact skin as a positive control, were taken. Then, the histological analysis was performed. In addition, a sample of tissue around the scar was collected and it was immediately immersed in a fixative solution consisting of 4 % neutral buffered formaldehyde, embedded in paraffin, and later sectioned at a thickness of 5 µm. The sections were stained with either hematoxylin and eosin (H&E) or picrosirius red (PSR). Stained sections were examined under a light microscope.

2.2.10. Statistical analysis

The Astatsa statistical calculator was used to carry out the statistical analyses. One-way analysis of variance (ANOVA) was followed by Scheffé for post-hoc comparisons. $p < 0.05$ was considered significant.

3. Results and discussion

3.1. Physico-chemical characterizations

The morphology of the scaffolds, before and after crosslinking, was analyzed by means of SEM (Fig. 1). The acquired images showed microparticles with a predominantly smooth surface, characterized by a spheroidal shape and the presence of concavities. No differences were observed related to the variation in the ratio between the two polymers. The incorporation of LDH was confirmed by the presence of hexagonal platelets, typical of the structure of this type of clay, visible on the outer portion of the microparticles (red arrows in Fig. 1), which led to a more uneven surface and a greater presence of collapsed microparticles. This may be related to the tendency of LDH to form submicron-sized aggregates which contribute to the modifications observed. Crosslinking with $CaCl_2$ did not affect the structural and morphological integrity. However, a slight increase in surface roughness was observed, probably due to the washing and centrifugation steps necessary for the recovery of the solid material.

Concerning the elemental analysis, the detection of sulfur (S) confirmed the presence of chondroitin sulfate within the structure, while calcium (Ca) is related to the successful formation of the "egg-box" complex with the alginate chains (Cao et al., 2020). The key elements of the clay structure (Zn, Al) were found in the doped microparticles.

As reported in Table 2, the mean diameters of the microparticles (d [4;3]) ranged between 10 and 17 µm, with a relatively narrow particle size distribution (Span <2). LDH-doped microparticles showed comparable (as in the case of the A2 and A2-LDH) or slightly larger (for A3 and A3-LDH samples) mean diameters. The doping with the inorganic material could result in a slight increase of the size of the structures. This is also visible after crosslinking, probably due to the formation of the "egg-box" structure and the partial aggregation of the particles, also confirmed by the SEM images above.

To further investigate the clays distribution within the polymeric structure, FIB-SEM analyses were performed and reported in Fig. 1. No differences were pointed out from a morphological point of view for the sections of both the blank and the doped samples: both presented spheroidal and collapsed microparticles with pores in the submicron range, probably related to the evaporation of residual solvent during the drying process (Zhang et al., 2020). The clay distribution in the doped microparticles was found to be uneven. In fact, the images showed LDH aggregates recognized by their typical lamellar structure, as evidenced by the red arrows. The linear elemental scan (Figure S1 of the Supplementary Information) further confirms the presence of LDH through the detection of the characteristic elements. In particular, the increase of elemental intensity of Zn and Al in specific areas was related to the presence of clay aggregates, proving the obtainment of the microsphere structure which is typical of clay-polymer composites (Constantino et al., 2023).

In addition, small-angle X-Ray scattering (SAXS) analysis was performed with the aim of elucidating the structural features of the microparticles and to evaluate the effects of LDH incorporation on their morphology and organization. The SAXS scattering profiles of A2 and A3 systems are reported in Fig. 2A and 2B, together with the intensity contribution of the individual components (ALG and CS). The intensity profiles of the complexes (both A2 and A3) differed significantly from the intensity calculated by adding the contributions of the two individual components. Data confirmed that ALG and CS interacted on the nanoscale, forming microparticles with a peculiar internal arrangement, a composite polymer matrix rather than a simple mixture of constituents.

The SAXS profiles of A2 and A3 revealed the characteristic structural features of the microparticles: at high values of the scattering vector q, corresponding to the very local arrangement of the polymers, both

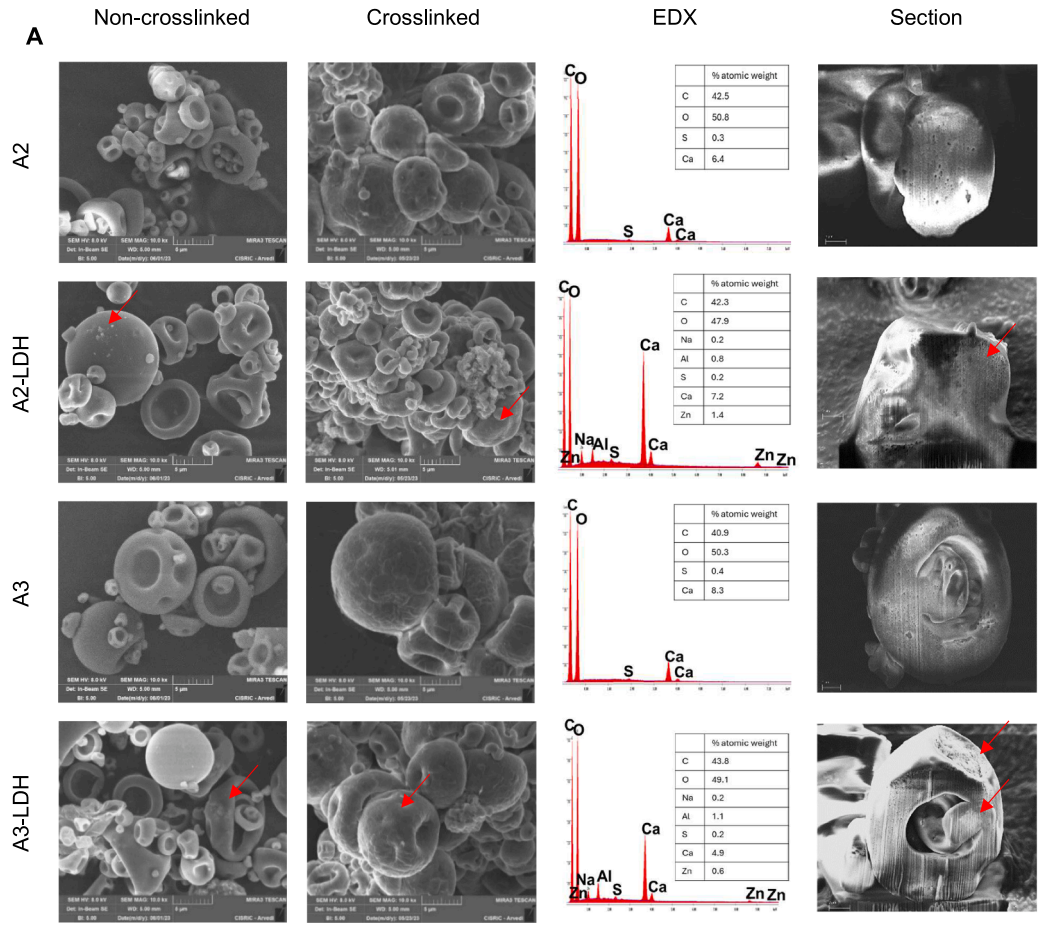

Fig. 1. SEM images of the non-crosslinked and crosslinked microparticles, EDX spectra and FIB-SEM images of the sections of the crosslinked microparticles. In the insets of the EDX spectra, the composition of the microparticles in atomic weight percentage.

Table 2
Statistical particle parameters of spray-dried non-crosslinked (c) and crosslinked (c) microparticles (mean values ± s.d; $n = 3$). Anova One-Way, Scheffé test, $p < 0.05$: d[4;3], A2 nc vs A2 c, A2-LDH c, A3-LDH nc, A3-LDH c; A2 c vs A2-LDH nc, A3 nc, A3 c, A3-LDH nc; A2-LDH nc vs A2-LDH c, A3-LDH nc, A3-LDH c; A2-LDH c vs A3 nc, A3 c, A3-LDH c; A3 nc vs A3 c, A3-LDH nc, A3-LDH c; A3 c vs A3-LDH c; A3-LDH nc vs A3-LDH c.

Sample		d10 (μm)	d50 (μm)	d90 (μm)	d[4,3] (μm)	Span
A2	nc	4.8 ±0.1	9.2 ± 0.4	20.7 ± 3.7	11.3 ± 1.3	1.3 ± 0.1
	c	5.2 ±0.2	11.8 ± 0.8	31.9 ± 4.9	15.5 ± 1.7	2.0 ± 0.1
A2-LDH	nc	4.7 ± 1.1	9.2 ± 0.3	21.2 ± 4.1	11.3 ± 1.1	1.6 ± 0.1
	c	5.3 ± 0.5	11.7 ± 1.6	29.2 ± 4.6	15.2 ± 1.7	1.8 ± 0.1
A3	nc	5.2 ± 0.1	9.4 ± 0.3	16.7 ± 1.1	10.2 ± 0.5	1.2 ± 0.1
	c	6.1 ± 0.1	11.8 ± 0.7	22.1 ± 2.0	13.1 ± 0.8	1.4 ± 0.1
A3-LDH	nc	5.4 ± 0.1	10.4 ± 0.2	22.7 ± 2.1	13.1 ± 1.2	1.6 ± 0.1
	c	5.4 ± 0.1	11.4 ± 0.4	35.4 ± 4.6	16.6 ± 1.8	2.0 ± 0.1

systems displayed a power-law dependence of I(q)≈ q^{-1}, which is indicative of elongated and straight polymer chains, until a q value of 0.79 nm^{-1}, corresponding to a maximum length of about 8 nm (Fig. 2C and 2D). This trend suggests that the mixed chains are less flexible on the very local length scale than a Gaussian polymer in good solvent, behaving as rigid chains at distances below 8 nm. In the low-q region, corresponding to distances within the microparticles of the order of hundreds of nanometers, the scattering curves followed a power-law dependence of I(q) ≈$q^{-3.5}$, characteristic of surface fractals, suggesting a complex morphological organization with irregular surface features. Furthermore, an intermediate-q peak was observed at $q = 0.06$ nm^{-1}, corresponding to a characteristic dimension of approximately 100 nm, which likely represents a repetitive distance between structural elements within the polymer network, such as crosslinking points or compact domains.

The analysis of the ZnAl LDH sample revealed a distinct peak at $q = 4.4$ nm^{-1}, corresponding to a periodic spacing of about d = 1.4 nm (Fig. 2E and 2F). This is consistent with the values reported in literature for the multi-layered structure of LDH (Iyi et al., 2007). When LDH were doped into the microparticles (A2-LDH and A3-LDH), the overall structure of the polymer matrix remained largely unchanged, as evidenced by the similarity of the SAXS profiles at low and intermediate-q (Fig. 2E and 2F). However, in the high-q region, the power-law dependence shifted from −1 to −1.3, indicating a more flexible arrangement of the polymer chains on the local length scale. The results suggested that the LDH incorporation subtly modulates the microstructural properties, softening the polymer matrix. The differences observed between samples with and without LDH highlight the interplay between the

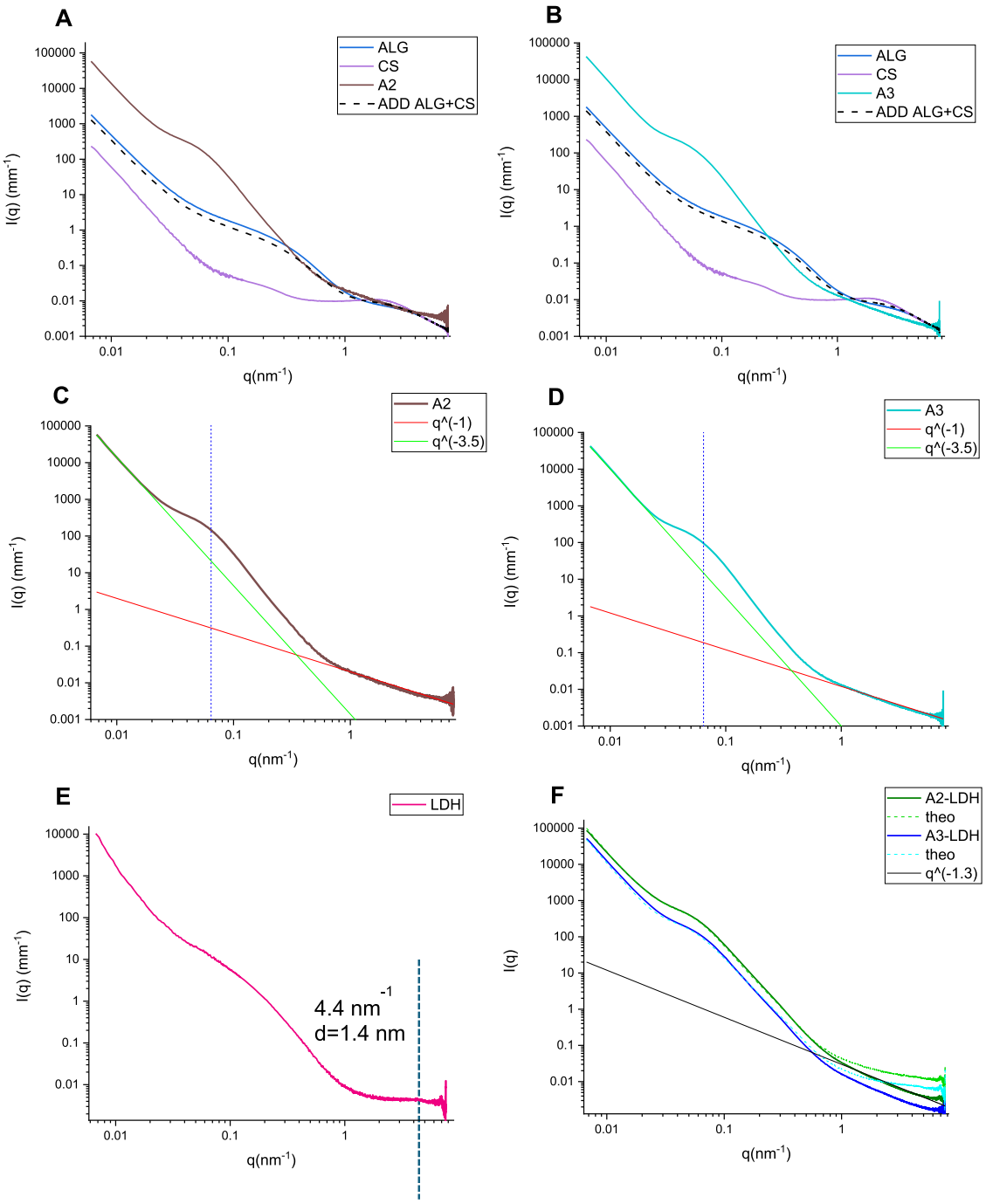

Fig. 2. (A, B) SAXS spectra of ALG, CS in comparison with A2 and A3 microparticles. The curve obtained by simply adding the contribution of the two individual components is represented in black dashed lines. (C, D) SAXS spectra of A2 and A3 microparticles. Straight lines represent the two different power-low of the scattered intensity decay: $I(q) \div q - 3.5$ (green line) in the low-q range, $I(q) \div q - 1$ for $q > 7.9 \times 10{-}1$ nm^{-1} (red line). The peak at 0.06 nm^{-1} is highlighted with a blue dashed line. (E) SAXS spectra of ZnAl LDH (pink line). The blue dashed line evidences the position of the characteristic peak linked to the distance between lamellae ($q = 4.4$ nm^{-1}). (F) SAXS spectra of A2-LDH and A3-LDH (respectively green and blue line), in comparison with theoretical curves obtained by adding the spectra of the two components (green and blue dashed lines). In black the straight line represents the power law q-1.3.

crosslinked polymer framework and the incorporated inorganic phase. While the addition of LDH does not disrupt the overall polymer architecture, it introduces localized changes that affect the material's mechanical properties at the nanoscale.

In summary, SAXS analysis revealed that A2 and A3 microparticles exhibit an internal structure characterized by an entangled compact polymer network, with surface-fractal arrangement, and with elongated chains on the very local scale. The LDH doping modified the local-scale flexibility of the composite without altering its mesoscopic organization. The presence of LDH lamellae with a characteristic spacing of 1.4 nm was confirmed, contributing to the nanoscale properties of the composite.

The XRD technique allowed the evaluation of the crystallinity of the samples due to presence of the clays. The patterns of the pure starting materials, alginate and chondroitin sulfate, are reported in Figure S2 of the Supplementary Information. The semi-crystalline structure of alginate and amorphous chondroitin sulfate was confirmed, as reported in the literature (Bhagyaraj & Krupa, 2020). In particular, three peaks were

clearly visible for pure alginate at values of 13.7°, 21.9°, 23.8° of 2θ (Venkatesan et al., 2012), while chondroitin sulfate had a very large peak at around 22° of 2θ. However, the intensity of the peaks related to alginate was reduced after spray drying due to the polymer amorphization, leading to broad reflections almost superimposable to those of chondroitin sulfate.

Fig. 3A shows the patterns obtained from the crosslinked microparticles and the pristine LDH based on Zn and Al. The LDH-doping in the microparticles was confirmed by the peaks at 11.3°, 22.7° and 60.8° of 2θ, corresponding to the d003, d006 and d110 reflections, respectively. However, the matching interlayer distances were different from the pure ZnAl LDH phase: in particular, values of 7.8 and 3.9 Å related to the d003 and d006 reflections were found, proving the intercalation of carbonate anions rather than nitrate. This phenomenon might have taken place during the suspension of LDH in water, either for the spray drying process or for the washing of the microparticles. Carbonate anions contained in water have higher affinity to the cationic layers compared to nitrate anions (Wang et al., 2024).

The FTIR spectra of pure alginate and chondroitin sulfate are shown in Figure S3 of the Supplementary Information. According to literature reports, sodium alginate shows characteristics broad absorption bands at around 3400 cm^{-1} (stretching vibrations of the hydroxyl groups), 2930 cm^{-1} (CH_2 stretching), 1590 cm^{-1} (asymmetric stretching vibration of COO groups), 1394 cm^{-1} (symmetric stretching vibration of COO groups), 1250, 1045 and 1018 cm^{-1} (elongation of C—O groups) (Helmiyati, 2017; Pereira et al., 2011). Concerning the fingerprint region, the bands at 930 and 895 cm^{-1} are assigned to the C—O stretching vibration, C—H deformation vibration of uronic acid residues, while the one at 804 cm^{-1} is typical of the mannuronic acid residues (Gómez-Ordóñez & Rupérez, 2011). For chondroitin sulfate, the overlapping stretching vibrations of −OH and N − H can be observed at approximately 3400 cm^{-1}, while the C − H stretching vibration of the methyl or methylene groups are visible at approximately 2930 cm^{-1}. The signals at 1600 and 1560 cm^{-1} indicate the presence of −NH−C = O groups in the structure, while the bands at 1376 and 1220 cm^{-1} represent the stretching vibrations of the $S = O$ bonds of the sulfate groups (Zhao et al., 2022; Xiong et al., 2021).

These characteristic bands mentioned above were also visible in the spectra of the crosslinked microparticles (Fig. 3B), given the prevalence of the organic products in the structures. The typical peak of LDH at approximately 1300 cm^{-1} was overlapped by the signals covering the range of 1400–1250 cm^{-1} given by the polymers. Therefore, these results were not completely informative in terms of LDH doping.

In Figure S4 of the Supplementary Information, the TGA and DSC profiles of pure alginate and chondroitin sulfate can be found. According to such results, sodium alginate showed a first mass loss starting from around 100 °C due to the loss of absorbed water, followed by the rupture of the glycosidic bonds (starting from approximately 210 °C), leading to alginate fragmentation. Then, starting from around 420 °C, the monomeric units of the alginate degraded into Na_2CO_3, which later decomposed rapidly, leaving a final residue of about 16 % (Flores-Hernández et al., 2021; Soares et al., 2004). For CS, the mass loss occurred in three primary stages: the first, until 160 °C, ascribed to the loss of CS water. The second, between 230 and 280 °C, attributed to the decomposition of CS associated with the release of sulfate groups and carboxylic acids (decomposition of uronic acid and pyranose units). The third, when

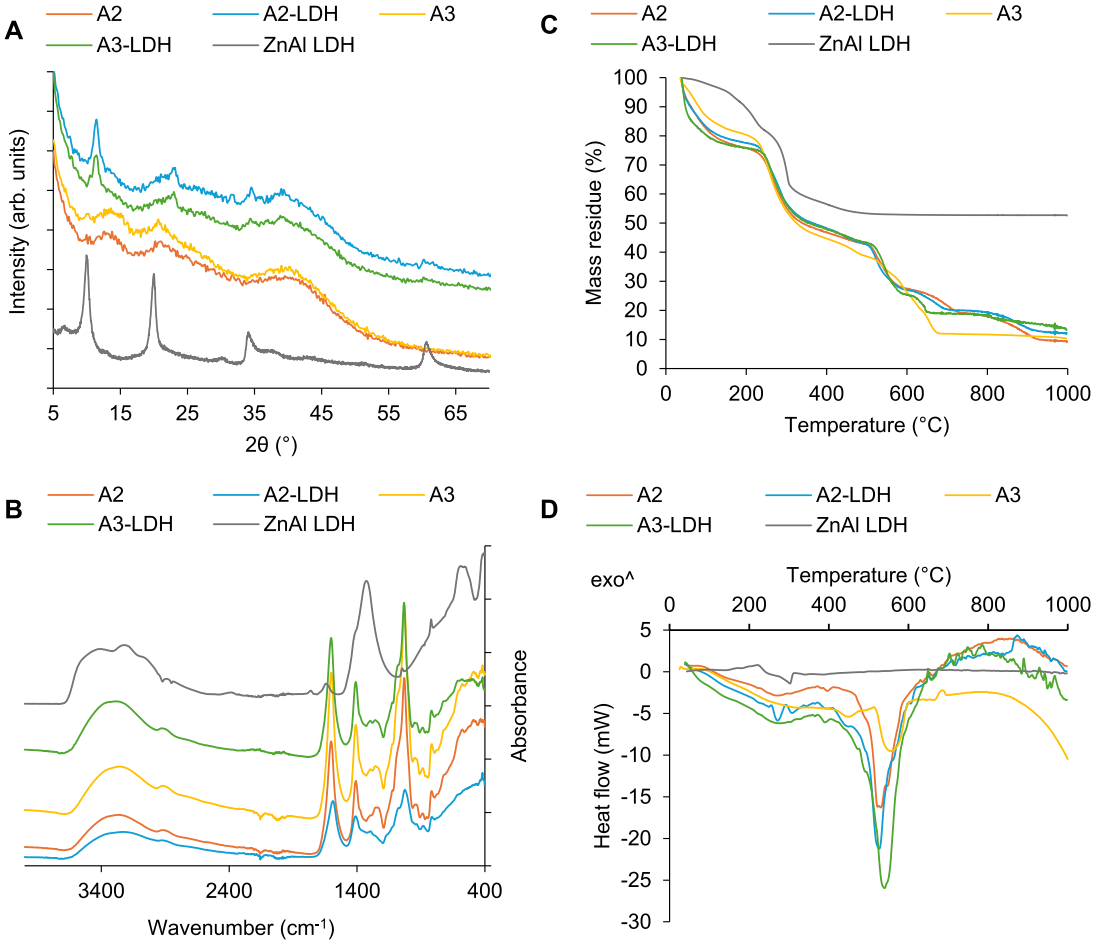

Fig. 3. XRD patterns (A), FTIR spectra (B), TGA (C) and DSC (D) profiles of the crosslinked microparticles and ZnAl LDH.

heated above 350–400 °C, related to the oxidative degradation of residual carbon and sulfur compounds (Zhao et al., 2022; Konovalova et al., 2020).

The TGA and DSC profiles of the microparticles and the ZnAl LDH are shown in Fig. 3C and 3D, respectively. The ZnAl LDH exhibited a four-stage weight reduction. A preliminary weight reduction was detected around 100 °C due to the loss of hydration water adsorbed on the cationic layers. Two further phases could then be identified up to 400 °C. These are mostly due to the dehydroxylation of the octahedral cationic layers, which results in the elimination of water molecules and the removal of nitrate ions from the interlamellar region (Kameda et al., 2010). The elimination of some residual impurities could be responsible for the final 5 % weight loss. On the other hand, the contribution of the organic polymers is mainly responsible for the thermal degradation of the microparticles, which showed a first rapid weight loss up to around 200 °C related to the elimination of water, mainly due to the portion of chondroitin sulfate. Then, a rapid degradation was observed around 200–240 °C, attributed to the fragmentation of ALG and CS. From 500 °C to 700 °C, the decomposition of the residual Na_2CO_3, carbon and sulfur moieties was visible. At the end of the analysis, the differences between the residues of the blank and doped microparticles confirmed the successful inclusion of LDH in the matrix. The DSC data corroborated the TGA results.

3.2. *In vitro degradation and Zn^{2+} release*

An in vitro degradation test was performed on the crosslinked microparticles to evaluate the stability of the scaffolds in their hydrated state. This is an essential investigation since a higher stability would better promote haemostasis and ensure a balance between exudate absorption and wound bed dehydration, both essential characteristics in the granulation phase of wound healing (Ruggeri et al., 2022)

As visible from the SEM micrographs reported in Fig. 4A, the morphology of the microparticles was maintained for up to 6 days, suggesting high stability and slow degradation. However, a greater morphological loss was observed for the A3 sample, probably due to the presence of a higher amount of alginate, which is therefore more easily subjected to degradation. For LDH-doped particles, the presence of clay agglomerates no longer included in the organic matrix could be spotted, which highlighted the degradation of the polymeric portion.

These findings are confirmed by the residual mass values of the samples after hydration (Fig. 4B). In general, a slow degradation for all types of microparticles was observed (the minimum residue obtained was around 66 % of the initial weight). The most pronounced weight loss of the LDH-doped microparticles could be linked to the simultaneous degradation of the inorganic portion, which over time undergoes the decomposition of the platelets, with consequent release of its components.

This was also demonstrated by the amount of Zn^{2+} ion, a promoter of skin regeneration, released over time (Fig. 4C). The profiles indicated a quantitative release after just three days. The A2-LDH microparticles showed a faster release over time than A3-LDH microparticles, and then both reached a comparable maximum amount released of about 32 % after 18 days. This is consistent with the type of clays that were considered, and the release medium used. The neutral pH of water allowed a slower degradation of the clays and a slower release of the inorganic elements, prolonging the beneficial effect that could be provided to chronic wounds.

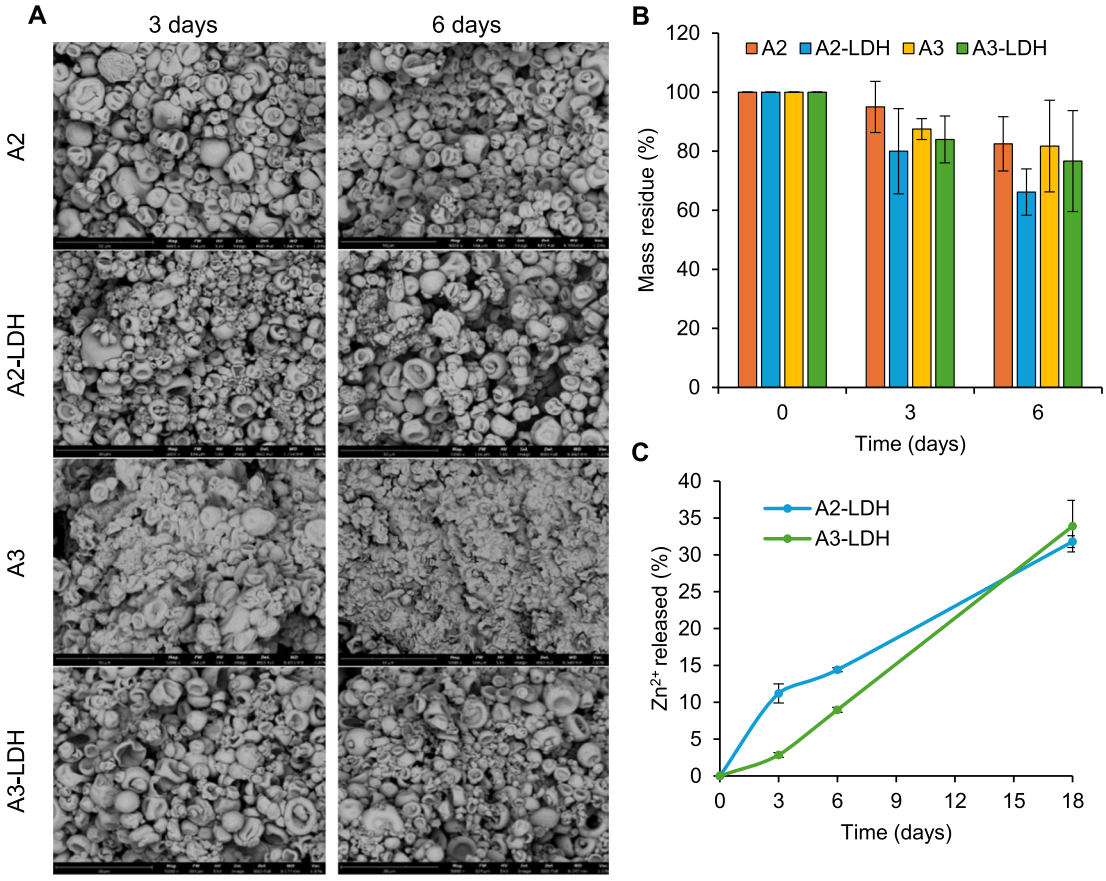

Fig. 4. (A) SEM images of the crosslinked microparticles after 3 and 6 days of degradation in water at 37 °C. (B) Mass residues (%) of the microparticles after the degradation test. (C) Zn^{2+} released from the LDH structure in the microparticles up to 18 days of degradation.

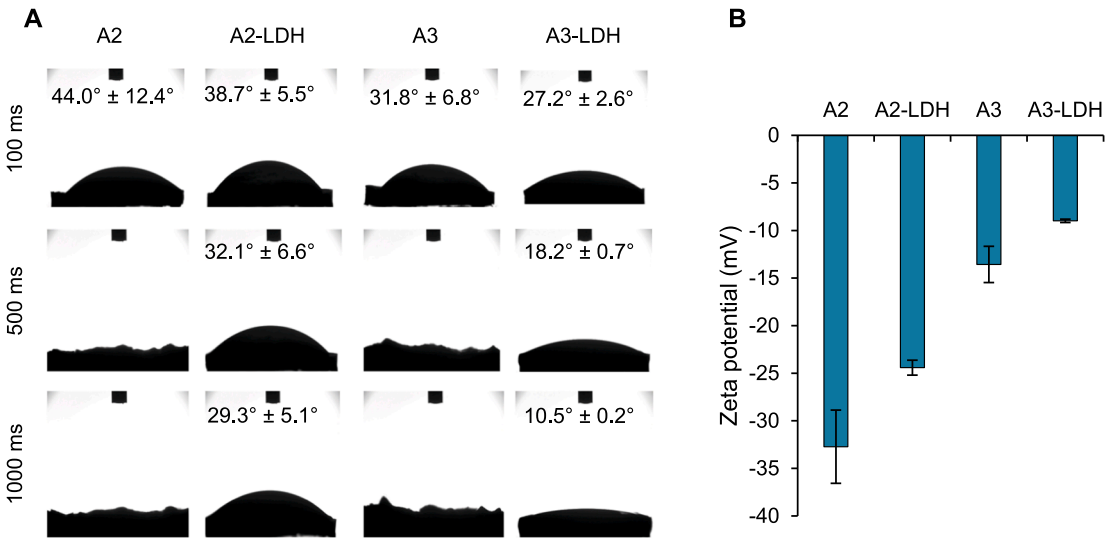

Fig. 5. (A) Images of the water droplet after 100, 500 and 1000 ms of contact with the surface of the scaffold. In the insets, the contact angle value is reported (mean values ± sd, $n = 3$). (B) Zeta potential of the microparticles at physiological pH (mean values ± sd, $n = 3$).

3.3. Contact angle and zeta potential measurements

The wettability of the scaffolds was assessed to investigate the behavior and hydrophilicity of these structures in a physiological environment. Fig. 5A shows the shape and contact angle values of a water droplet released on the surface of pressed disks obtained from the microparticles. Having a contact angle of $<90°$, scaffolds were predominantly hydrophilic, consistent with what is reported in the literature based on their composition (Tam et al., 2011). The presence of LDH resulted in reduced wettability with greater contact angles. In fact, the blank microparticles completely absorbed the liquid after 500 ms of contact with the liquid, causing even partial swelling. This did not occur in clay-doped structures, although the original hydrophilicity was still maintained. Therefore, the obtained data suggest that the inorganic portion could ensure greater stability of the microparticles in a physiological environment. Moreover, the A2-LDH microparticles led to higher hydrophobicity than A3-LDH. This may be due to the variation in the ratio between the polymers constituting the microparticles: in particular, the increase of alginate in the structure could confer a greater tendency to water absorption.

The apparent zeta potential (ζ) was determined to assess the possible interaction of the microparticles with cells and tissues at physiological pH (Fig. 5B). The surface charge of particles has been shown to affect cell viability. The negative zeta potential is one of the most decisive factors for biocompatible materials, which allow for greater cell viability as there is less risk of uncontrolled endocytosis (García-Villén et al., 2020).

Considering the weight ratio of the polymers and the presence of LDH, all microparticles presented a negative zeta potential value. This is consistent with the charge of the ionizable groups present in the polymeric structures and with the zeta potential values reported in the literature (Barbosa et al., 2019). In particular, the zeta potential increased for the A2 and A2-LDH particles, suggesting higher stability compared to the A3 and A3-LDH samples. This may be related to the higher amount of alginate (with lower negative charge density) than chondroitin sulfate (with higher negative charge density) in the A3/A3-LDH formulations, whose carboxyl groups were neutralized after crosslinking with Ca^{2+}. The doping of microparticles with LDH, whose zeta potential is positive, led to a slight decrease in the zeta potential, as expected, while overall maintaining negative values, which prove to be optimal for cell growth.

3.4. Cell proliferation

Cell proliferation was assessed using Normal Human Dermal Fibroblasts (NHDF). NHDF represent one of the most suitable cell-based models for the in vitro evaluation of scaffolds intended for the treatment of skin lesions, as they are the most abundant cell type in all connective tissues and play an important role in the wound healing process.

Cells grown in the presence of microparticles were characterized by fluorescence intensity (F.I.) values, directly related to the cell number. For all the concentrations examined, a statistically significant increase of F.I. was observed at each time interval, resulting in a cell proliferation increase which ranged from 10 to 15 % when compared to cells grown in standard conditions (Fig. 6). No statistical significance was observed after 6 days for cells treated with the undoped microparticles at the highest concentration (10 mg/ml), resulting in a proliferation increase of roughly 1–5 %. In addition, statistical significance was observed after 3 days for the undoped particles between the highest and lowest concentration (10 and 0.5 mg/ml). This may be due to the larger amount of the material seeded in the cell wells which slightly physically impaired cell proliferation. In general, the composition of the microparticles could be beneficial for cell proliferation due to the presence of alginate and chondroitin sulfate.

When in contact with the wound exudate, the calcium ions that are present in the alginate network may be exchanged with sodium ions, resulting in a partial swelling of the alginate structure This phenomenon limits wound secretions, while maintaining a physiologically moist microenvironment that promotes healing, supports granulation tissue formation, and reduces bacterial contamination (Sahana & Rekha, 2018; Lee et al., 2009). Moreover, alginate is also able to actively influence the pathophysiological mechanisms of chronic wounds by binding large amounts of inflammatory factors like IL-8 and TNF-α and inhibiting free radical formation in vitro (Wiegand & Hipler, 2010).

Sulfated glycosaminoglycans such as chondroitin sulfate can also have moisture-absorbing properties that contribute to wound closure (Shah et al., 2021). CS regulates the cascade of wound healing by interacting particularly with growth factors like FGF-2, favoring cell-cell and cell-substrate adhesion, increasing proliferation, and migration of fibroblast cells, initiating the cascade of the wound healing mechanism in diabetic wounds, partial- and full-thickness wounds. Moreover, CS regulates the levels of pro-inflammatory and inflammatory cytokines, suppresses the NF-κB pathway activation, enhances fibroblast activity, facilitates keratinocyte proliferation, and upregulates VEGF expression

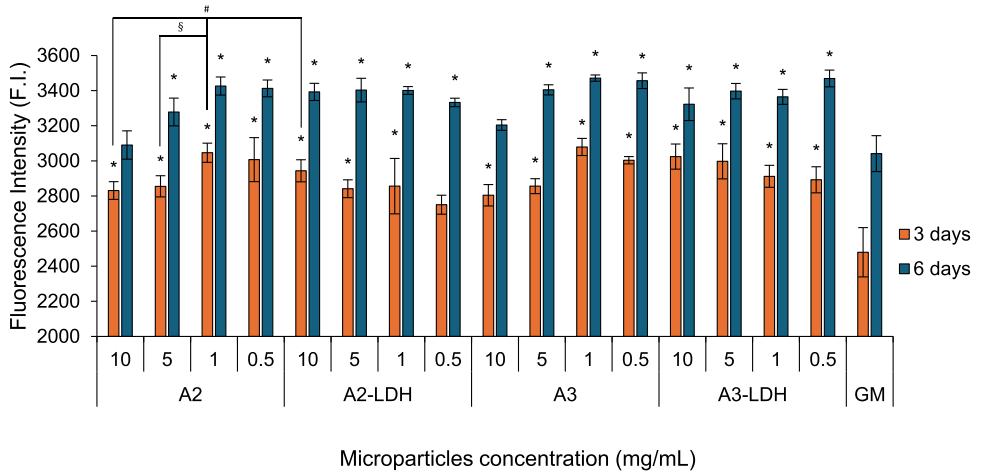

Fig. 6. Proliferation of Normal Human Dermal Fibroblasts after 3 and 6 days of contact with the microparticles (mean values ± sd, $n = 3$). Simbol * indicates statistical significance against control. Simbols # and § indicate statistical significance between the data groups indicated.

(Sharma et al., 2022; Mantry et al., 2024). More importantly, CS is also one of the constituents of the FDA-approved skin substitute Integra for treating burns, since it enhances re-epithelialization while reducing scar formation (Sharma et al., 2022).

The addition of ALG and CS improves the permeability and biodegradability of the scaffold, which is favorable for the diffusion of oxygen and nutrients to the cells. This, in turn, allows for more ECM deposition, thus enhancing tissue regeneration (Xiong et al., 2021; Little et al., 2014).

LDH also seemed to guarantee positive effects on cell viability and proliferation, as an increase in fluorescence intensity values was observed for the LDH-doped microparticles, in particular at the highest concentrations tested.

3.5. Safety and efficacy of the systems in vivo

The efficacy of the scaffolds was investigated in vivo by implanting them in full-thickness circular burn skin lesions. The saline-treated lesion (NaCl 0.9 %) was used as a control.

Fig. 7A shows the profiles of reduction of skin wound area (%) as a function of the time for scaffold-treated lesions (3, 6, 13 and 17 days). All scaffolds led to a greater reduction in wound area (%) compared to the control. By comparing the different samples and the control over the course of the experiment, differences in performance were observed. In fact, the mean wound area of A3 and A3-LDH formulations was reduced of around 36 and 48 % respectively against the control, suggesting the effectiveness of the formulations. The statistically significant wound area reduction of the lesions treated with A3-LDH could suggest its greater positive effect on wound healing compared to the other formulations.

Fig. 7B reports Hematoxylin and Eosin (H&E) and Picrosirius Red (PSR) staining of intact skin, subcutaneous implants of the microparticles, and the lesions (burns followed by excision) treated with saline solution as negative control and with spray-dried microparticles.

The subcutaneous implants were performed to study in vivo safety of the system. According to the histology of the tissues, all subcutaneous implants led to completely and correctly reformed epidermal layers, and the underlying connective tissue was also reconstituted. Dermal papillae and skin appendages were being properly reformed. After 17 days from the implantation, microparticles or aggregates were no longer detectable in the tissue depth. No evidence of inflammation or foreign body reaction was visible with H&E staining, indicating that all formulations were biocompatible in a murine model. After implantation of A2 and A3, the dermis was remodelled in its papillary and reticular parts. Picrosirius red stained red-orange collagen bundles, which were almost completely mature and arranged in a similar way to those of intact skin. Concerning the A2-LDH sample, the underlying connective tissue was forming dermal papillae and cutaneous appendages, and still showed some dilated capillaries and some residual granulation tissue. A small area was still lacking collagen bundles. The A3-LDH sample was not yet fully re-epithelialized for a stretch of about 8mm. Several dilated capillaries were evident in the dermis. In both cases, picrosirius red stained the yellow-orange collagen that was organizing itself into bundles.

Moreover, the efficacy of the microparticles to promote tissue regeneration was also evaluated. The A2-treated wound showed a completely re-epithelialized surface area, which was reforming papillae and appendages, even if it was still covered by strongly eosinophilic necrotic material for a small stretch. Inflammatory material was still found in the underlying dermis. Collagen was organizing itself into bundles, which were still partially formed. The staining with picrosirius red showed several thin bundles of collagen, colored green/yellow, of recent formation and not yet thickened and organized. In the sample treated with A2-LDH, a small (about 5 mm) stretch of surface was observed that was not yet completely covered by epithelium. A few small areas of superficial necrotic material persisted. There were no glands or hair follicles. The dermis had many capillaries that were still dilated (neoangiogenesis) and collagen bundles that were not yet organized. At specific staining with picrosirius red the collagen appeared immature, green-yellow with only a few orange bundles.

Samples A3 and A3-LDH showed a similar regenerative process, with a small (about 5 mm and 7 mm, respectively) tract on the surface not yet covered by epithelium and protected by eschar. In both samples, the dermis was in the inflammatory phase and showed several dilated blood vessels. Collagen bundles were in the process of being formed and organized. Picrosirius red showed differences, with the newly formed collagen staining green-yellow for A3 and red-orange for A3-LDH.

On the contrary, the lesions treated with saline solution were still covered by acidophilic necrotic material with not re-epithelialized epidermis. Inflammatory cells and several dilated capillaries were still present in the underlying dermis. In addition, dermal papillae or skin appendages were not visible.

Overall, wounds treated with all microparticles showed signs of proliferative phase of healing, demonstrating that the regeneration process was accelerated in wounds treated with microparticles compared to saline solution, which highlighted signs of inflammatory phase. In particular, the wounds treated with A3-LDH showed the more advanced regenerative step, as the collagen already showed sign of remodelling.

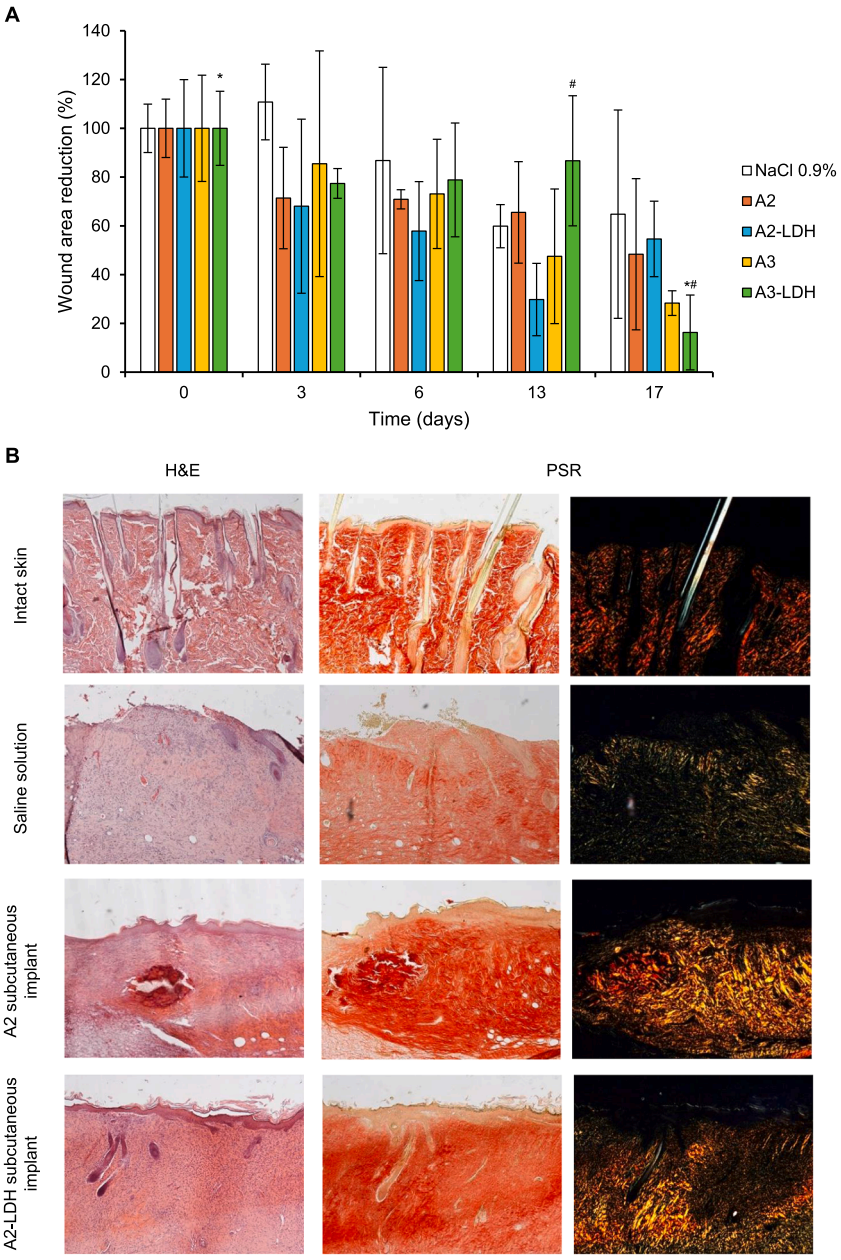

Fig. 7. (A) Wound area reduction (%) over time of the lesions treated with the scaffolds (3, 6, 13, 17 days), compared with control (saline solution NaCl 0.9 %) (mean values ± sd, $n = 3$). Simbols * and # indicate statistical significance. (B) H&E (left panel) and PSR (central panel - with bright-field images; right panel - with polarized light) sections of intact skin, lesions treated with saline solution, subcutaneous implants of the microparticles, lesions treated with the microparticles ($n = 3$). Original magnification: 5X. Each micrograph frame has a width of 1780 μm.

4. Conclusions

Microparticles prepared using alginate and chondroitin sulfate in different ratios were manufactured using the spray drying technique and successfully crosslinked using $CaCl_2$. They were also doped with layered double hydroxides (LDH) made of Zn and Al, which were produced using the coprecipitation method. Spheroidal particles with mean diameters ranging 10–15 μm were obtained, which were maintained after the doping and crosslinking process. A narrow dimensional distribution was obtained, as evidenced by the low polydispersion (Span values lower than 2). Physico-chemical and solid-state analyses confirmed the clay doping, with TGA analysis showing a residue of around 5 %w/w related to the LDH presence. Clays conferred better stability on the scaffold in an aqueous environment as evidenced by the increased wettability of the systems, which could enhace their potential as promoters of the wound healing process. In addition, the microparticles demonstrated controlled release of Zn^{2+} ions, reaching up to 35 % release over 18 days, directly correlating to their ability to induce fibroblast proliferation. Comparing the formulations, both A3 and A3-LDH showed better performance, with an increasing in vitro fibroblast proliferation rate of up to 15 % and reduction of the wound area in vivo of around 40 % compared to the control. The likely synergistic effect of the combination of the polysaccharides and LDH seemed to enhance both structural stability of the scaffold and its regenerative potential. This composite scaffold seems therefore promising for the enhancement of wound healing. Moreover, the materials and the processes used could further implement the industrial production of this scaffold facilitating the treatment of chronic wounds.

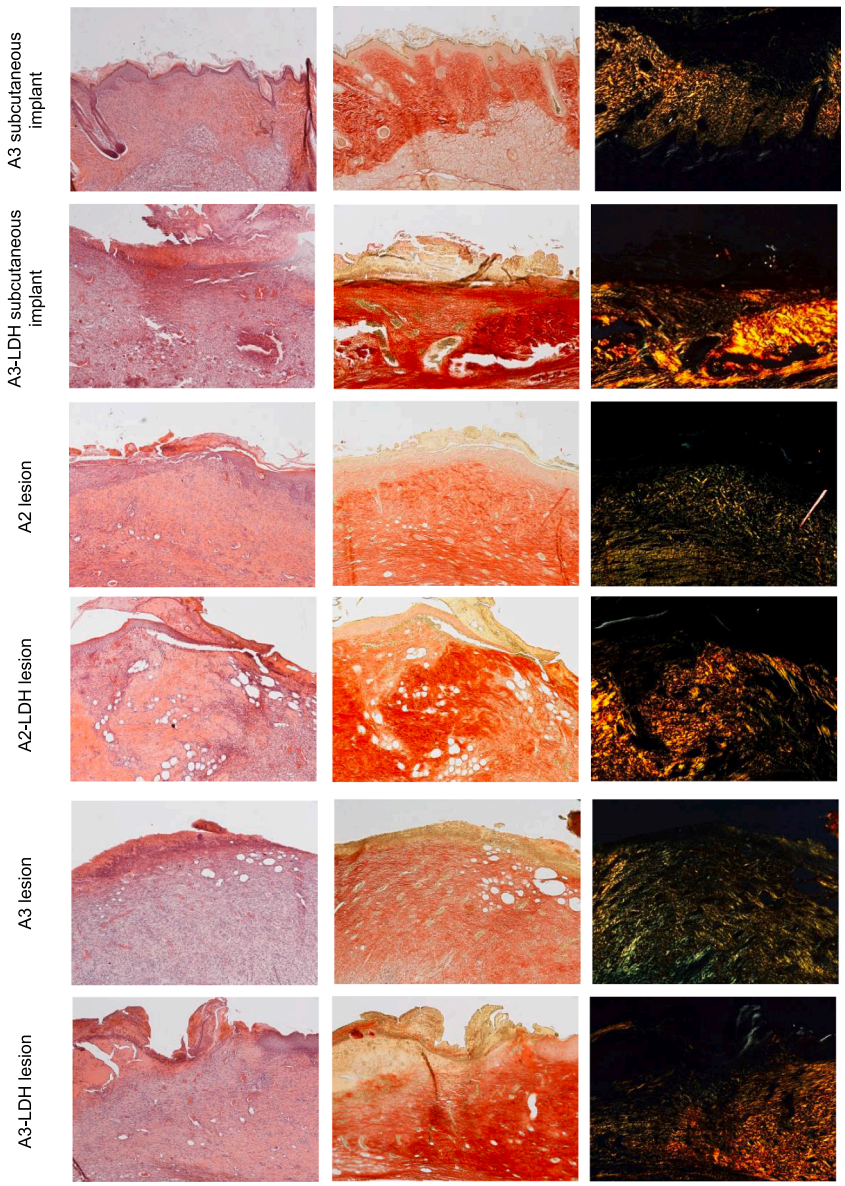

Fig. 7. (*continued*).

CRediT authorship contribution statement

Cristian Nomicisio: Writing – review & editing, Writing – original draft, Methodology, Investigation, Formal analysis, Data curation. **Marco Ruggeri:** Supervision, Methodology. **Christine Taviot-Guého:** Resources. **Cinzia Boselli:** Investigation. **Antonia Icaro Cornaglia:** Investigation. **Eleonora Bianchi:** Investigation. **Elena Del Favero:** Writing – original draft, Resources. **Caterina Ricci:** Writing – original draft, Resources. **Giuseppe Firpo:** Resources, Investigation. **Barbara Vigani:** Visualization. **Paolo Vacca:** Resources. **César Viseras:** Visualization. **Silvia Rossi:** Resources. **Giuseppina Sandri:** Writing – review & editing, Project administration, Funding acquisition, Conceptualization.

Declaration of competing interest

The authors declare that they have no known competing financial interests or personal relationships that could have appeared to influence the work reported in this paper.

Acknowledgements

CN thanks Programma Operativo Nazionale Ricerca e Innovazione (PON R&I 2014–2020, REACT-EU FSE DM 1061/2021) and SAES Getters SpA for his PhD position. The authors acknowledge ESRF (Grenoble, Fr) for beamtime allocation and financial support for x-ray experiments (doi: 10.15151/ESRF-ES-653835676) and ID02 staff for precious technical assistance. The authors thank the animal facility "Centro di servizio per la gestione unificata delle attività di stabulazione e di radiobiologia" of the University of Pavia (Italy) to host the animals and the OPBA of the University of Pavia for support in animal protocol drawing up.

Supplementary materials

Supplementary material associated with this article can be found, in the online version, at doi:10.1016/j.carpta.2025.100711.

Data availability

Data will be made available on request.

References

Heras, K. Las, Igartua, M., Santos-Vizcaino, E., & Hernandez, R. M. (2020). Chronic wounds: Current status, available strategies and emerging therapeutic solutions. *Journal of Controlled Release, 328*, 532–550. https://doi.org/10.1016/j.jconrel.2020.09.039

Pei, J., Palanisamy, C. P., Alugoju, P., Anthikapalli, N. V. A., Natarajan, P. M., Umapathy, V. R., Swamikannu, B., Jayaraman, S., Rajagopal, P., & Poompradub, S. (2023). A comprehensive review on bio-based materials for chronic diabetic wounds. *Molecules (Basel, Switzerland), 28*, 604. https://doi.org/10.3390/molecules28020604

Molina, M. I. E., Malollari, K. G., & Komvopoulos, K. (2021). Design challenges in polymeric scaffolds for tissue engineering. *Frontiers in Bioengineering and Biotechnology, 9*, Article 617141. https://doi.org/10.3389/fbioe.2021.617141

Nosenko, M. A., Moysenovich, A. M., Zvartsev, R. V., Arkhipova, A. Y., Zhdanova, A. S., Agapov, I. I., Vasilieva, T. V., Bogush, V. G., Debabov, V. G., Nedospasov, S. A., Moisenovich, M. M., & Drutskaya, M. S. (2018). Novel biodegradable polymeric microparticles facilitate scarless wound healing by promoting re-epithelialization and inhibiting fibrosis. *Frontiers in Immunology, 9*, 2851. https://doi.org/10.3389/fimmu.2018.02851

Dong, J., Cheng, Z., Tan, S., & Zhu, Q. (2021). Clay nanoparticles as pharmaceutical carriers in drug delivery systems. *Expert Opinion on Drug Delivery, 18*, 695–714. https://doi.org/10.1080/17425247.2021.1862792

Mousa, M., Evans, N. D., Oreffo, R. O. C., & Dawson, J. I. (2018). Clay nanoparticles for regenerative medicine and biomaterial design: A review of clay bioactivity. *Biomaterials, 159*, 204–214. https://doi.org/10.1016/j.biomaterials.2017.12.024

Ruggeri, M., Nomicisio, C., Taviot-Guého, C., Vigani, B., Boselli, C., Grisoli, P., Icaro Cornaglia, A., Bianchi, E., Viseras, C., Rossi, S., & Sandri, G. (2024). Smart copper-doped clays in biomimetic microparticles for wound healing and infection control. *Materials Today Bio, 29*, Article 101292. https://doi.org/10.1016/j.mtbio.2024.101292

Miele, D., Ruggeri, M., Vigani, B., Viseras, C., Natali, F., Favero, E. D., Rossi, S., & Sandri, G. (2023). Nanoclay-doped electrospun nanofibers for tissue engineering: Investigation on the structural modifi. *International Journal of Nanomedicine, 18*, 7695–7710. https://doi.org/10.3390/ijms13056102

Rajeshkumar, G., Arvindh Seshadri, S., Ramakrishnan, S., Sanjay, M. R., Siengchin, S., & Nagaraja, K. C. (2021). A comprehensive review on natural fiber nano-clay reinforced hybrid polymeric composites: Materials and technologies. *Polymer Composites, 42*, 3687–3701. https://doi.org/10.1002/pc.26110

Ghadiri, M., Chrzanowski, W., & Rohanizadeh, R. (2015). Biomedical applications of cationic clay minerals. *RSC Advances, 5*, 29467–29481. https://doi.org/10.1039/C4RA16945J

Ameena Shirin, V. K., Sankar, R., Johnson, A. P., Gangadharappa, H. V., & Pramod, K. (2021). Advanced drug delivery applications of layered double hydroxide. *Journal of Controlled Release, 330*, 398–426. https://doi.org/10.1016/j.jconrel.2020.12.041

Nomicisio, C., Ruggeri, M., Bianchi, E., Vigani, B., Valentino, C., Aguzzi, C., Viseras, C., Rossi, S., & Sandri, G. (2023). Natural and synthetic clay minerals in the pharmaceutical and biomedical fields. *Pharmaceutics, 15*, 1368. https://doi.org/10.3390/pharmaceutics15051368

Hu, T., Gu, Z., Williams, G. R., Strimaite, M., Zha, J., Zhou, Z., Zhang, X., Tan, C., & Liang, R. (2022). Layered double hydroxide-based nanomaterials for biomedical applications. *Chemical Society Reviews, 51*, 6126–6176. https://doi.org/10.1039/D2CS00236A

Constantino, V. R. L., Figueiredo, M. P., Magri, V. R., Eulálio, D., Cunha, V. R. R., Alcântara, A. C. S., & Perotti, G. F. (2023). Biomaterials based on organic polymers and layered double hydroxides nanocomposites: Drug delivery and tissue engineering. *Pharmaceutics, 15*, 413. https://doi.org/10.3390/pharmaceutics15020413

Lee, S. L., O'Connor, T. F., Yang, X., Cruz, C. N., Chatterjee, S., Madurawe, R. D., Moore, C. M. V., Yu, L. X., & Woodcock, J. (2015). Modernizing pharmaceutical manufacturing: From batch to continuous production. *Journal of Pharmaceutical Innovation, 10*, 191–199. https://doi.org/10.1007/s12247-015-9215-8

ICH guideline Q13 on continuous manufacturing of drug substances and drug products EMA/6401/2023, (2023). https://www.ema.europa.eu/en/ich-guideline-q13-continuous-manufacturing-drug-substances-and-drug-products-scientific-guideline (accessed January 31, 2025).

Nomicisio, C., Taviot-Guého, C., Ruggeri, M., Forano, C., Vigani, B., Viseras, C., Rossi, S., & Sandri, G. (2024). Layered double hydroxides for biomedical purposes: Sustainable and green synthesis. *Applied Clay Science, 258*, Article 107480. https://doi.org/10.1016/j.clay.2024.107480

Ma, W., Zhang, J., Shu, L., Tan, X., An, Y., Yang, X., Wang, D., & Gao, Q. (2020). Optimization of spray drying conditions for the green manufacture of γ-aminobutyric acid-rich powder from Lactobacillus brevis fermentation broth. *Biochemical Engineering Journal, 156*, Article 107499. https://doi.org/10.1016/j.bej.2020.107499

Sosnik, A., & Seremeta, K. P. (2015). Advantages and challenges of the spray-drying technology for the production of pure drug particles and drug-loaded polymeric carriers. *Advances in Colloid and Interface Science, 223*, 40–54. https://doi.org/10.1016/j.cis.2015.05.003

Sahoo, D. R., & Biswal, T. (2021). Alginate and its application to tissue engineering. *SN Applied Sciences, 3*, 30. https://doi.org/10.1007/s42452-020-04096-w

Wu, G., Ma, F., Xue, Y., Peng, Y., Hu, L., Kang, X., Sun, Q., Ouyang, D. F., Tang, B., & Lin, L. (2022). Chondroitin sulfate zinc with antibacterial properties and anti-inflammatory effects for skin wound healing. *Carbohydrate Polymers, 278*, Article 118996. https://doi.org/10.1016/j.carbpol.2021.118996

Dazon, C., Taviot-Guého, C., & Prévot, V. (2023). Layered double hydroxides: Where should research stress on for massive scaling up? *Materials Advances, 4*, 4637–4645. https://doi.org/10.1039/D3MA00478C

Lin, P.-H., Sermersheim, M., Li, H., Lee, P. H. U., Steinberg, S. M., & Ma, J. (2017). Zinc in wound healing modulation. *Nutrients, 10*, 16. https://doi.org/10.3390/nu10010016

Cui, S., Yao, B., Gao, M., Sun, X., Gou, D., Hu, J., Zhou, Y., & Liu, Y. (2017). Effects of pectin structure and crosslinking method on the properties of crosslinked pectin nanofibers. *Carbohydrate Polymers, 157*, 766–774. https://doi.org/10.1016/j.carbpol.2016.10.052

Cao, L., Lu, W., Mata, A., Nishinari, K., & Fang, Y. (2020). Egg-box model-based gelation of alginate and pectin: a review. *Carbohydrate Polymers, 242*, Article 116389. https://doi.org/10.1016/j.carbpol.2020.116389

Zhang, S., Wu, D., & Zhou, L. (2020). Characterization of controlled release microspheres using FIB-SEM and image-based release prediction. *AAPS PharmSciTech, 21*, 194. https://doi.org/10.1208/s12249-020-01741-w

Iyi, N., Fujii, K., Okamoto, K., & Sasaki, T. (2007). Factors influencing the hydration of layered double hydroxides (LDHs) and the appearance of an intermediate second staging phase. *Applied Clay Science, 35*, 218–227. https://doi.org/10.1016/j.clay.2006.08.011

Bhagyaraj, S., & Krupa, I. (2020). Alginate-mediated synthesis of hetero-shaped silver nanoparticles and their hydrogen peroxide sensing ability. *Molecules (Basel, Switzerland), 25*. https://doi.org/10.3390/molecules25030435

Venkatesan, J., Pallela, R., Bhatnagar, I., & Kim, S.-K. (2012). Chitosan–amylopectin/hydroxyapatite and chitosan–chondroitin sulphate/hydroxyapatite composite scaffolds for bone tissue engineering. *International Journal of Biological Macromolecules, 51*, 1033–1042. https://doi.org/10.1016/j.ijbiomac.2012.08.020

Wang, Y., Ying, Z., Gao, Y., & Shi, L. (2024). Layered double hydroxide nanosheets: Synthesis strategies and applications in the field of energy conversion. *Chemistry - A European Journal, 30*, Article e202303025. https://doi.org/10.1002/chem.202303025

Helmiyati, M. A. (2017). Characterization and properties of sodium alginate from brown algae used as an ecofriendly superabsorbent. *IOP Conference Series: Materials Science and Engineering., 188*, Article 012019. https://doi.org/10.1088/1757-899X/188/1/012019

Pereira, R., Tojeira, A., Vaz, D. C., Mendes, A., & Bártolo, P. (2011). Preparation and characterization of films based on Alginate and Aloe Vera. *International Journal of Polymer Analysis and Characterization, 16*, 449–464. https://doi.org/10.1080/1023666X.2011.599923

Gómez-Ordóñez, E., & Rupérez, P. (2011). FTIR-ATR spectroscopy as a tool for polysaccharide identification in edible brown and red seaweeds. *Food hydrocolloids, 25*, 1514–1520. https://doi.org/10.1016/j.foodhyd.2011.02.009

Zhao, Y., Li, Y., Lan, T., Wang, B., Huang, M., Huang, H., Qiao, C., & Sun, J. (2022). Fabrication and characterization of chicken- and bovine-derived chondroitin sulfate/sodium alginate hybrid hydrogels. *Gels, 8*, 620. https://doi.org/10.3390/gels8100620

Xiong, X., Xiao, W., Zhou, S., Cui, R., Xu, H. H. K., & Qu, S. (2021). Enhanced proliferation and angiogenic phenotype of endothelial cells via negatively-charged alginate and chondroitin sulfate microsphere hydrogels. *Biomedical Materials, 16*, Article 025012. https://doi.org/10.1088/1748-605X/abd994

Flores-Hernández, C. G., Cornejo-Villegas, M. D. L. A., Moreno-Martell, A., & Del Real, A. (2021). Synthesis of a biodegradable polymer of poly (Sodium Alginate/Ethyl Acrylate). *Polymers, 13*, 504. https://doi.org/10.3390/polym13040504

Soares, J. P., Santos, J. E., Chierice, G. O., & Cavalheiro, E. T. G. (2004). Thermal behavior of alginic acid and its sodium salt. *Eclética Química, 29*, 53–56. https://doi.org/10.1590/S0100-46702004000200009

Konovalova, I., Novikov, V., Kuchina, Y., & Dolgopiatova, N. (2020). Technology and properties of chondroitin sulfate from marine hydrobionts. In *, 2020. International Applied Research Conference «Biological Resources Development and Environmental Management* (pp. 305–314). https://doi.org/10.18502/kls.v5i1.6075

Kameda, T., Fubasami, Y., Uchiyama, N., & Yoshioka, T. (2010). Elimination behavior of nitrogen oxides from a NO3−-intercalated Mg–Al layered double hydroxide during thermal decomposition. *Thermochimica Acta, 499*, 106–110. https://doi.org/10.1016/j.tca.2009.11.009

Ruggeri, M., Vigani, B., Boselli, C., Icaro Cornaglia, A., Colombo, D., Sànchez-Espejo, R., Del Favero, E., Mandras, N., Roana, J., Cavallo, L., Cantù, L., Viseras, C., Rossi, S., & Sandri, G. (2022). Smart nano-in-microparticles to tackle bacterial infections in skin tissue engineering. *Materials Today Bio, 16*, Article 100418. https://doi.org/10.1016/j.mtbio.2022.100418

Tam, S. K., Dusseault, J., Bilodeau, S., Langlois, G., Hallé, J.-P., & Yahia, L. (2011). Factors influencing alginate gel biocompatibility. *Journal of Biomedical Materials Research Part A, 98A*, 40–52. https://doi.org/10.1002/jbm.a.33047

García-Villén, F., Faccendini, A., Miele, D., Ruggeri, M., Sánchez-Espejo, R., Borrego-Sánchez, A., Cerezo, P., Rossi, S., Viseras, C., & Sandri, G. (2020). Wound healing activity of Nanoclay/spring water hydrogels. *Pharmaceutics, 12*, 467. https://doi.org/10.3390/pharmaceutics12050467

Barbosa, J. A. C., Abdelsadig, M. S. E., Conway, B. R., & Merchant, H. A. (2019). Using zeta potential to study the ionisation behaviour of polymers employed in modified-release dosage forms and estimating their pKa. *International Journal of Pharmaceutics: X, 1*, Article 100024. https://doi.org/10.1016/j.ijpx.2019.100024

Sahana, T. G., & Rekha, P. D. (2018). Biopolymers: Applications in wound healing and skin tissue engineering. *Mol Biol Rep, 45*, 2857–2867. https://doi.org/10.1007/s11033-018-4296-3

Lee, W., Park, J., Kim, K., Kim, S., Park, D., Chae, M., Suh, S., Jeong, S., & Park, K. (2009). The biological effects of topical alginate treatment in an animal model of skin wound healing. *Wound Repair Regeneration, 17*, 505–510. https://doi.org/10.1111/j.1524-475X.2009.00496.x

Wiegand, C., & Hipler, U.-C. (2010). Polymer-based biomaterials as dressings for chronic stagnating wounds. *Macromolecular Symposia, 294*, 1–13. https://doi.org/10.1002/masy.200900028

Shah, S. A., Sohail, M., Khan, S. A., & Kousar, M. (2021). Improved drug delivery and accelerated diabetic wound healing by chondroitin sulfate grafted alginate-based thermoreversible hydrogels. *Materials Science and Engineering: C, 126*, Article 112169. https://doi.org/10.1016/j.msec.2021.112169

Sharma, R., Kuche, K., Thakor, P., Bhavana, V., Srivastava, S., Mehra, N. K., & Jain, S. (2022). Chondroitin sulfate: Emerging biomaterial for biopharmaceutical purpose and tissue engineering. *Carbohydrate Polymers, 286*, Article 119305. https://doi.org/10.1016/j.carbpol.2022.119305

Mantry, S., Behera, A., Pradhan, S., Mohanty, L., Kumari, R., Singh, A., & Yadav, M. K. (2024). Polysaccharide-based chondroitin sulfate macromolecule loaded hydrogel/scaffolds in wound healing- A comprehensive review on possibilities, research gaps, and safety assessment. *International Journal of Biological Macromolecules, 279*, Article 135410. https://doi.org/10.1016/j.ijbiomac.2024.135410

Little, C., Kulyk, W., & Chen, X. (2014). The effect of chondroitin sulphate and hyaluronic acid on chondrocytes cultured within a fibrin-alginate hydrogel. *JFB, 5*, 197–210. https://doi.org/10.3390/jfb5030197